Preferred citation: T. Tuovinen, J. Jeronen and P. Becker. Simulation of sloshing of condensate water inside a drying cylinder using particle finite element method. In **Advances in Pulp and Paper Research, Oxford 2017**, *Trans. of the XVIth Fund. Res. Symp. Oxford, 2017*, (W. Batchelor and D. Söderberg, eds), pp 383–407, FRC, Manchester, 2018. DOI: 10.15376/frc.2017.1.383.

SIMULATION OF SLOSHING OF CONDENSATE WATER INSIDE A DRYING CYLINDER USING PARTICLE FINITE ELEMENT METHOD

Tero Tuovinen, Juha Jeronen and Pablo Becker

ABSTRACT

Energy consumption is a key issue in paper making due to its high costs and for ecological reasons. In this paper, we focus on the simulation of the drying section, with a special emphasis on the heat transfer inside a steam-heated drying cylinder, accounting for the sloshing of condensate water inside the cylinder. It is known that the condensate creates a barrier reducing the efficiency of heat transfer through the cylinder surface, a shortcoming that can be overcome by the addition of turbulator bars that increase the convective heat transfer through the water layer. In this study, we simulate the fluid flow and heat transfer in the drying roll for both the water and steam phase, but for simplicity, neglect the phase change. The Particle Finite Element Method with a fixed mesh (PFEM-2) is used to compute the numerical solution. Our aim is to show the capability of this method for solving complex sloshing phenomena with adequate qualitative accuracy and computational efficiency.

Key words: Papermaking, Drying, Simulation, PFEM-2.

1 INTRODUCTION

As is well known, the traditional way of drying paper during its production process is to use heated cylinders. It is a convenient, reliable and economical process, because in the production of pulp, parts of the raw material have been extracted and can be burnt as a source of energy. In the process, hot steam under pressure is conducted to the inside of each drying cylinder. The main idea is that the phase change of steam into liquid water releases heat to the inner surface of the cylinder, increasing its temperature. This heat is then transferred to the wet paper by conduction through the cylinder, thereby drying the product in contact with the outer surface.

However, there are practical issues associated with this approach, one of which this study concentrates on. Condensed water accumulates inside the cylinder, and the viscous forces inside the liquid phase during the rolling cause the water to rise around the rim of the cylinder; see the schematic in Figure 2.1. At high rotational speeds, the water develops a heat-insulating barrier layer around the inner rim of the cylinder in a phenomenon known as rimming, making the heat transfer process inefficient. To reduce this layer, turbulator bars are installed along the inner rim of the cylinder, helping to increase the mixing and sloshing of the fluid, thus improving the heat transfer by introducing convection in the condensate layer.

With turbulator bars installed, most of the water becomes restricted in condensate pools, the size of which can be adjusted by choosing the distance between adjacent bars when the cylinder is designed. Moreover, one can choose this distance so that the wave's eigenfrequency inside the pool is equal to the rotational frequency of the cylinder. In that case, wave energy increases rapidly, making the sloshing more turbulent. The mixing of water increases, therefore improving the efficiency of heat transfer due to the increase in convection through the thickness of the water layer.

Previously, studies into the sloshing dynamics and the heat transfer rate of the condensate layer have been made using various methods, for example, in [1, 2, 3, 4, 5, 6, 7, 8, 9]. In [6, 7], the case of a cylinder with a scraper has been studied both experimentally and analytically. The installation of turbulator bars inside the cylinder dramatically improves the heat transfer rate from the steam to the shell of the cylinder, and provides a more uniform heat profile on the cylinder shell [10]. However, the situation becomes difficult to analyze without experimentation, due to the complicated motion of the water sloshing between the bars. Numerous studies have been made in the more general case of water sloshing inside a container concerning its dynamics, see e.g. [11, 12, 13, 14]. The points of interest are usually the shape of the free surface, and the mechanical load experienced by the walls.

Beside [6, 7], and a study into the effect of oscillation on the heat transfer rate of liquid [15], little progress has been reported in deriving accurate heat transfer

rates in analytical and/or numerical studies applicable to the case at hand. In [16], heat transfer with rotating bars has been studied, but only in the outside region.

The aim of the present study is to evaluate the usability of a second-generation Particle Finite Element Method (PFEM) on this kind of problems, and to gain a first insight about the transient behavior of the system. PFEM is extension of traditional Lagrangian FEM (finite element method), but with more flexibility to handle free-boundary problems and discontinuities between multi-phase flows, both of which may be crucial in later stages of this study.

Fluid flows are commonly considered in an Eulerian setting, i.e. the physical quantities such as the flow velocity and pressure are mathematically considered as properties of points in the laboratory coordinate system. However, Lagrangian formulations, traditionally used in solid mechanics, offer a better choice for simulations where deformations cannot be neglected, such as in multi-phase problems [17].

Lagrangian formulations provide the great advantage that each particle or node has its own properties and advects (transports) them through the domain, therefore reducing or almost eliminating numerical diffusion [17]. PFEM consists of using a set of particles that define the nodes of a FEM mesh. Since fluids have no deformation limit, remeshing must be done at each time step, creating new connectivities and possibly new nodes. Otherwise the elements can become too distorted or even inverted [17]. As an example, in [18] PFEM was used to simulate several interacting fluids with temperature coupling for the analysis of magmatic chambers. Thermally coupled PFEM has been employed also for the simulation of industrial applications; see e.g. [19, 20]. An advantage of PFEM is that since there is no need to define a function to track the interface, the number of phases is unlimited without any modifications; each particle simply carries the properties of the associated material. For example, it is possible to analyze the wave generation caused by a landslide in dams [21], using as many phases as needed.

Algorithms combining both Eulerian and Lagrangian approaches have proved to be a good alternative to pure methods. A recent enhancement of the PIC (particle-in-cell) method is the so called Particle Finite Element Method second generation (PFEM-2) with fixed mesh [22]. This method consists of using a fixed FEM mesh, and particles that are used to estimate the solution, by integrating along the streamlines defined by the fixed mesh. The corrections needed are minimal and the accuracy of the solver is excellent for a given mesh size. Moreover, since streamlines are followed in a Lagrangian fashion, there is no limitation on the time step. The length of the time step is only limited by the required precision.

In this work, we investigate the sloshing phenomenon from a fundamental academic perspective, focusing on a two-dimensional model. We restrict our study to the movement and sloshing of the condensate and to the heat transfer. We

do not consider the renewal of the steam, the phase change between steam and water, or the heat transfer through the cylinder into the paper web. Results for different initial configurations will be analyzed.

The model employs the PFEM-2 particles to store and convect all the properties, both thermal and mechanical (fluid). For the temperature problem, the heat transfer equation is split into two unknowns, namely the water and steam temperature. This splitting allows to have better control on the details of the model (see section 4.1), and reduces the error in a problem that is particularly challenging due to the moving phase interface and the high density difference between the liquid water and the steam.

The fluid flow problem is solved using an enhanced implementation of the PFEM-2 fluid solver. In this work, we solve the flow equations using a fictitious force approach based on a non-inertial frame co-rotating with the cylinder.

2 PROBLEM SETUP

In a classical cylinder-based dryer section of a paper machine, hot pressurized steam is led into horizontally rotating cylinders. The steam heats the inner surface of each cylinder. The heat transfers by conduction through the cylinder shell, and the outer surface of the cylinder heats the paper web travelling on the outside, in order to help remove moisture. The cooling steam forms condensate (liquid water), which, as the cylinder rotates, is driven by friction and centrifugal forces to form a layer on the inner surface of the cylinder, greatly reducing the heat transfer rate between the steam and the metal shell.

To improve the heat transfer, turbulator bars have been installed onto the inner surface of the cylinder. The bars are high enough so that the water does not freely flow over them, breaking the layer of condensate into smaller pools separated by the bars. As the cylinder rotates, the periodic change in the relative direction of gravity causes the water to slosh inside the pools. The spacing of the bars is chosen such that the sloshing occurs near the natural sloshing frequency regardless of the running speed of the cylinder. This resonance causes the sloshing to be violent, leading to chaotic behavior and turbulence. The resultant efficient mixing of water improves the heat transfer rate.

The aim of this research is to develop a simplified numerical model that simulates the transfer of heat inside a drying cylinder. Specifically, we investigate the transfer rate from the steam to the inner shell of the cylinder. To achieve this, the sloshing behavior of the condensate must be captured.

In the present study, it is assumed that steam is not renewed, and therefore it will cool down as the simulation advances in time. The level of condensate is assumed to be constant; in an actual cylinder, condensate is removed by a siphon

and new condensate is continuously formed. For simplicity, both of these effects are neglected here.

Let us consider the problem in detail. As heat is released from the steam inside the cylinder, the steam will cool down, and begin condensing on the inner surface, releasing the latent heat involved in the phase change, thus contributing to the heat transfer. However, as was already mentioned, the condensate water forms a layer on the inner shell of cylinder. Water is a poor conductor of heat, and an unbroken layer of water decreases the heat transfer rate between the steam and the cylinder shell significantly.

Consider a simple drying cylinder without turbulator bars. As the cylinder starts up from rest, the water condensing from the steam initially forms a puddle at the bottom, as shown in Figure 2.1. This is called the ponding phase. As the cylinder begins to rotate, friction drives water to follow the rising inner wall of the cylinder, with some of the water completing the rotation and some falling back down again. This is known as the cascading phase. It is characterized by violent and unpredictable behaviour of the water. As the rotational speed increases, eventually all the water completes the rotation. The water now completely covers the inside of the cylinder. In this rimming phase (also shown in Figure 2.2), the surface of the water is relatively undisturbed. In the study [23], these different phases and the timing of their appearance has been analyzed with several different condensate layer thicknesses, via a signal collected from the power source of rotating machinery.

In the ponding phase, the upper parts of the cylinder are mostly uncovered by condensate, resulting in a good heat transfer rate. In the cascading phase, the heat transfer is also improved by the turbulent behavior of the water. In the rimming phase, the surface of the water does not break, and the flow becomes laminar. Initially there is a gravity-driven sloshing motion associated with the water losing kinetic energy while climbing the wall, and gaining it while descending. This is prominent right as the phase shifts from cascading to rimming (at a speed known as the rimming speed). As the rotational speed of the cylinder increases, the flow becomes more and more dominated by centrifugal forces, and the depth of the water layer varies very little over a full rotation. The result is a flow in which the velocity component normal to the surface is very small, and thus forced convection from the free surface to the bottom practically vanishes. The heat transfer is now dominated by heat conduction.

Unfortunately, given the typical axial speed of a paper machine and the radius of a drying cylinder, steady operation occurs at a rotational speed that is above the rimming speed. Thus engineering solutions to significantly increase the heat transfer rate in rimming conditions are needed in practice.

A typical solution is to install bars onto the inner surface of the cylinder shell, their primary purpose being that they break up the water surface, and force the

motion of the water to become turbulent. The bars form open containers, which confine the water into separate small pools, rather than allowing it to flow freely around the perimeter of the cylinder. The periodic change in the direction of gravity that the water inside each container experiences causes the water to slosh between the bars, running up against one side as the container is rising, and up against the other side as it is descending.

Intuitively, as violent a sloshing as possible is desired, due to the increased turbulence it entails. Thus one wishes to set the bars at such a distance from each other that the sloshing occurs as close to the natural frequency of the container as possible. It turns out that the desired spacing is possible regardless of the operational speed of the cylinder, as the optimal distance only depends on the cylinder radius R and the depth δ of the (undisturbed) condensate.

Let us assume that in each pool, the situation can be simplified to that of a partially filled rectangular container. This assumption is justified if the bar spacing s is much less than the cylinder circumference $2\pi R$. Then the natural angular frequency of the sloshing is

$$\omega_n = \sqrt{gk \tanh(k\delta)}, \tag{2.1}$$

where g is the gravitational acceleration (SI unit [m/s^2]), k is the wavenumber (in radians per meter, i.e., [1/m]), and δ [m] is the depth of the undisturbed condensate.

The wavenumber of is a function of the pool length, width, and mode of oscillation. In the first oscillatory mode, the wavelength of the antisymmetric wave is twice the length of the container; then $k = \pi/s$ (where the unit of s is [m]), see e.g. [11].

In practice, the difficulty lies in achieving the condensate depth δ for a given installation. The depth depends not only on the condensing load, but also on the installation itself, namely the number of bars and their geometry. For details, see [3].

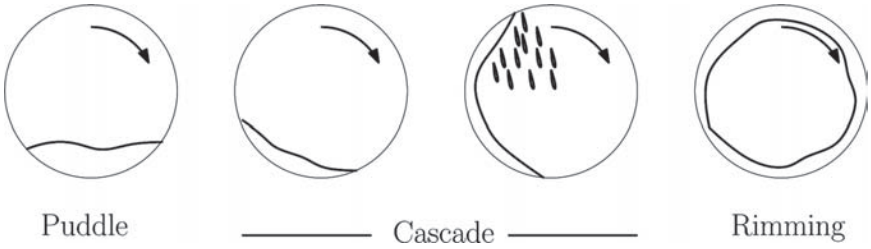

Figure 2.1. Condensate behavior at different rolling speeds.

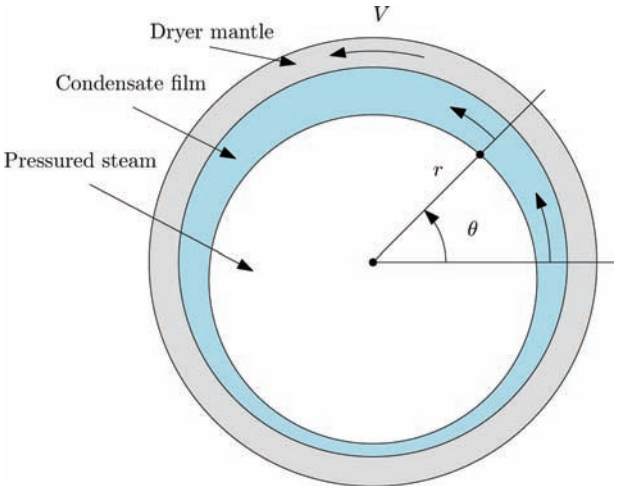

Figure 2.2. Condensate film inside of rolling dryer cylinder without turbulator bars.

3 GOVERNING EQUATIONS

3.1 Fluid flow

We have developed a strategy for the analysis of flows inside a rotating cylinder by solving the Navier – Stokes equations formulated with respect to a non-inertial reference frame (see section 4.3). The governing equations contain additional force terms respect to the standard Navier–Stokes equations, but the boundary conditions at rigid walls remain as simple no-slip conditions. A viscous fluid must move with the solid boundary, and hence the relative velocity of the fluid with respect to the contained must vanish at the container walls [9].

The equations of motion of an incompressible Newtonian liquid inside a rotating cylinder are (see e.g. [24])

$$\nabla \cdot \mathbf{u} = 0 \qquad \text{in } \Omega, \tag{3.1}$$

$$\frac{\partial \mathbf{u}}{\partial t} + \frac{1}{2}\nabla(\mathbf{u}\cdot\mathbf{u}) + (\nabla \times \mathbf{u}) \times \mathbf{u} + 2\boldsymbol{\Omega} \times \mathbf{u}$$
$$+ \boldsymbol{\Omega} \times (\boldsymbol{\Omega} \times \mathbf{r}) + \frac{\partial \boldsymbol{\Omega}}{\partial t} \times \mathbf{r} = -\frac{1}{\rho}\nabla p - \frac{\mu}{\rho}\nabla \times (\nabla \times \mathbf{u}) + \mathbf{F} \qquad \text{in } \Omega, \tag{3.2}$$

where Ω is the angular velocity of the rotating frame (with direction given by the right-hand rule), and all other quantities are given with respect to the rotating

frame. Here **u** is the fluid particle velocity [m/s], ***r*** the position [m], ρ the fluid density [kg/m^3], μ the dynamic viscosity [kg/(ms)], and **F** the body force vector [N].

It is possible to characterize the situation inside of the cylinder using the dimensionless similarity number K and the Reynolds number Re,

$$K = \frac{|\Omega|^2 R}{g}, \qquad \mathrm{Re} = \frac{|\Omega| R^2}{v}, \tag{3.3}$$

where Re characterizes the viscosity, and K the ratio of gravitational to rotational effects. Here R [m] is the radius of the cylinder, and $v = \mu/\rho$ ([m^2/s]) denotes the kinematic viscosity of the liquid, where μ is the dynamic viscosity as above.

Experimental tests of fluid behaviour in drying cylinders can be found in [25]. The qualitative behavior of the simulations can be compared to these results. In practical applications, the interest is mainly on the high values of the K, because it dominates the process time.

From a purely mechanical point of view, the liquid water dominates over the steam due to its much higher density. In fact, in many applications with high density ratios such as this one, the gaseous phase can often be completely neglected without sacrificing accuracy. However, it must be noted that one of the main goals of this simulation is to evaluate the heat transfer between the hot steam and the condensate layer. With this in mind, in this work the liquid and gas phases will be simulated simultaneously, using a two-phase fluid solver. This allows to capture correctly the movement of both phases, and therefore the heat transferred by convection.

Finally, in order to correctly model the problem, the density variation due to temperature changes must be taken into account. A variable density is particularly important in the steam phase, since it has a direct effect in the convection due to buoyancy. Given the relatively small range of temperatures analyzed, and for the sake of simplicity, in this work two assumptions will be made:

- The gaseous phase will be modelled as superheated dry steam. This allows to use the ideal gas law to obtain the steam properties, without the need of tables or further variables such as saturation.
- The steam will be modelled using the Boussinesq approximation; the volume will be considered constant, but the density will be computed using the ideal gas model.

Under these assumptions, both the liquid and gas phases will be modeled as incompressible fluids, but with variable density. This allows to capture the convection produced by the combination of the variable density and the movement of the drying cylinder.

3.2 Thermal convection and conduction

It is known that the increase of the thickness of the condensate rim inside the cylinder adversely affects heat transfer to the cylinder shell, reducing efficiency. In [26], experimental results of various water loads in a single 60-in diameter dryer are reported, at speeds up to 610 m/min. In [27], and later in [28], experimental evaluations of condensate effects have been made at speeds up to 1220 m/min, also including the effect of the turbulator bars added to improve the heat transfer during operation. Based on the findings from these studies, it is clear that the removal of the condensate is a critical part of the operation, affecting both the torque drive requirements during startup, and the heat transfer during operation. [25]

In the simulations, we have used the linear advection–diffusion equation to model the thermal convection and conduction:

$$c_p \rho \frac{\partial T}{\partial t} = \nabla \cdot (D \nabla T) - c_p \rho \nabla . (\mathbf{u} T) \qquad \text{in} \, \Omega, \tag{3.4}$$

where T is the temperature [K], D the thermal diffusivity [m^2/s], c_p [J/(kg K)] the specific heat at constant pressure, and ρ the density [kg/m^3]. The specific heat and diffusion coefficients for both phases are considered constant due to the small temperature variations. On the other hand, the densities computed for the solution of the fluid problem are used in this step.

It must be noted that our model does not currently allow for phase change. This means that in order to stay in the range of validity of the simulation, the temperature of the steam must always be above the boiling point of water at the conditions inside the drum.

4 PARTICLE FEM 2nd GENERATION (PFEM-2)

In the PFEM-2 strategy, problems are solved by splitting the equations into two steps. To begin with, all the properties are stored in particles without connectivities. The first step consists of computing the new position of the particles by using an explicit, high order spatial approximation by integrating the velocity in space. The main difference between PFEM-2 and other splitting methods is that while performing the advection, contributions to the main unknown can also computed and added continuously in space [22]. This technique is known as explicit streamline integration. For example, as particles are being advected, the velocity of the particle can be modified due to viscosity.

Having advected and added the explicit contributions to the particles, results are projected onto a fixed mesh, and the remaining part of the equation is solved.

After this step the splitting algorithm is complete, requiring only to send the information back to the particles to finish the time step.

For stability purposes, in this work a first-order splitting PFEM-2 will be used for both the heat transfer and fluid problems. This is due to the very high density ratio between the phases. Diffusive terms computed for the water phase on the fixed mesh would not represent the correct physical behavior in the steam phase, leading to unstable results. Therefore all the results presented in this work were simulated using the streamlines only to compute the new position, while the mesh is used to compute all the other terms using a backward Euler scheme.

Then the algorithm at each step becomes:

1. Advect the particles using streamlines computed on the mesh,
2. Project information onto the mesh,
3. Compute steam and water density,
4. Detect interface elements,
5. Assemble and solve fluid system of equations,
6. Assemble and solve thermal system of equations,
7. Update particles' velocity and temperature,
8. Reseed particles in empty elements of the mesh.

4.1 The thermal problem

Using the PFEM-2 strategy, the position and temperature of a particle p can be expressed as

$$\mathbf{x}_p^{n+1} = \mathbf{x}_p^n + \int_n^{n+1} \mathbf{V}_p^t(\mathbf{x}_p^t)\,\mathrm{d}t, \tag{4.1}$$

$$T_p^{n+1} = T_p^n + \int_n^{n+1} (\mathrm{d}T/\mathrm{d}t_p)^t(\mathbf{x}_p^t)\,\mathrm{d}t. \tag{4.2}$$

Using the PFEM-2 first order splitting described in the previous section, the strategy will consist on first advecting the particles and then computing the diffusive terms in the final configuration (on the finite element mesh):

$$\mathbf{x}_p^{n+1} = \mathbf{x}_p^n + \int_n^{n+1} \mathbf{V}_p^n(\mathbf{x}_p^t)\,\mathrm{d}t, \tag{4.3}$$

$$T_p^{n+1} = T_p^n + \Delta t \cdot (\mathrm{d}T/\mathrm{d}t_p)^{n+1}(\mathbf{x}_p^{n+1}). \tag{4.4}$$

The use of particles for the convection eliminates the advective term from (3.4), thus obtaining a transient pure diffusion equation to be solved in the mesh at each time step:

$$c_p \rho \frac{\partial T}{\partial t} = \nabla \cdot (D \nabla T) \qquad \text{in } \Omega. \tag{4.5}$$

At this stage it must be highlighted that there are two distinct phases in the simulation. Given the high density and diffusion difference between the steam and the condensate, the information exchange between the mesh and the particles must guarantee that energy is conserved. Furthermore, a single element of the mesh can contain both water and steam particles without a clear interface definition, thus making it difficult to define a single temperature on each node or element.

In order to overcome these limitations, two distinct temperatures will be defined on the mesh: the water temperature and steam temperature. This allows to solve two heat transfer equations, with good control on the properties of each phase. Moreover, writing the two equations separately allows to control and monitor the heat transfer at the interfaces between them. The equations to be solved become

$$\begin{aligned} c_{p,\mathrm{w}} \rho'_{\mathrm{w}} \frac{\partial T_{\mathrm{w}}}{\partial t} &= \nabla \cdot (D_{\mathrm{w}} \nabla T_{\mathrm{w}}) + Q \qquad \text{in } \Omega, \\ c_{p,\mathrm{s}} \rho'_{\mathrm{s}} \frac{\partial T_{\mathrm{s}}}{\partial t} &= \nabla \cdot (D_{\mathrm{s}} \nabla T_{\mathrm{s}}) - Q \qquad \text{in } \Omega, \end{aligned} \tag{4.6}$$

where the subscript w corresponds to the properties of the water phase, and s to those of the steam phase.

When a sharp interface is detected inside an element, an exact integration is performed by partitioning the element into sub-elements and assigning the corresponding density on each side of the interface; see [29, 30]. However, when the particle distribution does not present a defined interface, the element will be considered as a homogeneous continuum, in which, for a phase i, the density is computed as $\rho'_i = \rho_i \, n_i$, where n_i is the volume fraction of i within the element and $n_{\mathrm{w}} + n_{\mathrm{s}} = 1$.

The term Q [W/kg] controls the heat flow between the two phases. In this work, we use a simple model of the shape

$$Q = C \, l \, (T_{\mathrm{s}} - T_{\mathrm{w}}) \tag{4.7}$$

where C (unit [W / (kg K m)]) is the heat transfer coefficient between the water and steam phases, and l [m] is the length of the interface. For sharp interfaces, l can be computed exactly, while in diffuse mixture elements it will be set as $l = \sqrt{n_{\min} \, V_e}$, where $n_{\min} = \min \{n_{\mathrm{w}}, n_{\mathrm{s}}\}$ and V_e is the volume of the element. In other words, we assume there is a square shaped interface inside the element.

4.2 The fluid problem for a general case

Using again the PFEM-2 framework, the position and the velocity of a particle p can be expressed as

$$\mathbf{x}_p^{n+1} = \mathbf{x}_p^n + \int_n^{n+1} \mathbf{V}_p^t(\mathbf{x}_p^t)\,\mathrm{d}t, \tag{4.8}$$

$$\mathbf{V}_p^{n+1} = \mathbf{V}_p^n + \int_n^{n+1} \mathbf{a}_p^t(\mathbf{x}_p^t)\,\mathrm{d}t. \tag{4.9}$$

The previous equations are strongly coupled, since the accelerations depend on the position of each particle, and vice versa. Instead of solving both equations monolithically, we use the explicit approximation of PFEM-2 to compute $\mathbf{x}_p^{n+1}$. On the other hand, the velocity will be approximated using only the acceleration in the updated configuration $\mathbf{x}_p^{n+1}$. Therefore, the new position and velocity of a particle become

$$\mathbf{x}_p^{n+1} = \mathbf{x}_p^n + \int_n^{n+1} \mathbf{V}_p^n(\mathbf{x}_p^t)\,\mathrm{d}t, \tag{4.10}$$

$$\mathbf{V}_p^{n+1} = \mathbf{V}_p^n + \Delta t \cdot \mathbf{a}_p^{n+1}(\mathbf{x}_p^{n+1}). \tag{4.11}$$

This combination of explicit computation of the position together with an implicit strategy for the velocity automatically yields a segregated strategy. We use the particles to advect the unknowns and the required material properties. Having done this, the results are transferred into a continous domain, discretized using linear finite elements, and in this domain the velocity equation is solved. The fluid momentum equation equation is closed with a mass conservation equation, together yielding the non-stationary Stokes equations. Then the algorithm for incompressible fluids can be expressed as:

1. Advect particles (equation (4.10)),
2. Transfer data to mesh,
3. Solve the Stokes equations with additional non-inertial terms.

Once the change in velocity is computed by solving the Stokes equations, the particles' velocities are updated and the fluid flow problem is finished for this time step.

It must be noted that there is a single set of particles, which store both the fluid and thermal variables. Therefore, the advection of the particles (step 1) is performed only once per time step, and then the remaining parts of the heat transfer problem and the fluid problem are solved separately.

4.3 Fictious force approach

The rotating motion of the cylinder can be treated by introducing a non-inertial reference frame, whose origin stays fixed at all times t, but the frame undergoes an imposed rotating motion around the origin. For the sake of clarity, let us briefly review the details.

A non-inertial frame can be otherwise treated in the same manner as an inertial frame, except that we add some extra force terms to describe the inertial effects that arise from the accelerating motion (including rotational motion) of the non-inertial coordinate system (see e.g. [31]). These added terms represent a fictitious force. The name comes from the fact that this is not a true force in the sense of Newton's third law. Because the fictitious force arises purely due to geometry (kinematics), it has no equal and opposite reaction.

The rotation of the non-inertial frame is described by the vector $\boldsymbol{\Omega}$, pointing along the axis of rotation, with orientation given by the right-hand rule, and with magnitude (in radians per second, i.e., [1/s])

$$|\boldsymbol{\Omega}| = \omega(t). \tag{4.12}$$

For our application, we will concentrate mostly on the special case of rotation around the z axis,

$$\boldsymbol{\Omega} = (\Omega_1, \Omega_2, \Omega_3) = (0, 0, \omega). \tag{4.13}$$

The function $\omega(t)$ is considered given, describing the angular velocity of the cylinder.

Consider the true physical acceleration experienced by a material point. In the inertial coordinate system (let us denote it as frame A), this is written simply as

$$\boldsymbol{a} \equiv \frac{\mathrm{d}^2 x}{\mathrm{d}t^2} = \frac{\mathrm{d}^2}{\mathrm{d}t^2}\left(\sum_{j=1}^{3} \tilde{x}_j \hat{\boldsymbol{e}}_j\right) = \sum_{j=1}^{3} \tilde{a}_j \hat{\boldsymbol{e}}_j, \tag{4.14}$$

because the standard Cartesian basis vectors $\hat{\boldsymbol{e}}_j$, representing the axes of frame **A**, remain constant in time. The tilde reminds us that the components $\tilde{x}_j$ and $\tilde{a}_j$ are expressed in frame A.

On the other hand, we may also write this same acceleration in the non-inertial, rotating coordinate system (frame B). Let us denote the unit vector describing the jth axis (j = 1, 2, 3) of frame B by $\hat{\boldsymbol{u}}_j$. Due to the rotating motion of frame B, these basis vectors are time-dependent, $\hat{\boldsymbol{u}}_j = \hat{\boldsymbol{u}}_j(t)$. We have (see e.g. [32])

$$\boldsymbol{a} = \frac{\mathrm{d}^2}{\mathrm{d}t^2}\left(\sum_{j=1}^{3} x_j \hat{\boldsymbol{u}}_j\right) = \sum_{j=1}^{3} a_j \hat{\boldsymbol{u}}_j + 2\sum_{j=1}^{3} v_j \frac{\mathrm{d}\hat{\boldsymbol{u}}_j}{\mathrm{d}t} + \sum_{j=1}^{3} x_j \frac{\mathrm{d}^2 \hat{\boldsymbol{u}}_j}{\mathrm{d}t^2} \tag{4.15}$$

where the components a_j, v_j and x_j are expressed in frame B. The last form is obtained in the straightforward manner by applying d/dt twice. The time derivative of $\hat{\boldsymbol{u}}_j\,(t)$ is [33]

$$\frac{\mathrm{d}\hat{\boldsymbol{u}}_j}{\mathrm{d}t} = \Omega \times \hat{\boldsymbol{u}}_j \,. \tag{4.16}$$

Recall that in Cartesian component form, the cross product of any 3D vectors **u** and **v** is

$$\boldsymbol{u} \times \boldsymbol{v} = (u_2 v_3 - u_3 v_2, u_3 v_1 - u_1 v_3, u_1 v_2 - u_2 v_1). \tag{4.17}$$

The second time derivative of $\hat{\boldsymbol{u}}_j\,(t)$ is obtained by applying the operator d/dt to both sides of (4.16), and then rewriting the d$\hat{\boldsymbol{u}}_j$/dt term on the right-hand side of the result using (4.16). We have

$$\frac{\mathrm{d}^2 \hat{\boldsymbol{u}}_j}{\mathrm{d}t^2} = \frac{\mathrm{d}\Omega}{\mathrm{d}t} \times \hat{\boldsymbol{u}}_j + \Omega \times \frac{\mathrm{d}\hat{\boldsymbol{u}}_j}{\mathrm{d}t} = \frac{\mathrm{d}\Omega}{\mathrm{d}t} \times \hat{\boldsymbol{u}}_j + \Omega \times [\Omega \times \hat{\boldsymbol{u}}_j]. \tag{4.18}$$

Inserting equations (4.16) and (4.18) for the time derivatives of the unit vectors of frame B into equation (4.15), we obtain that the true physical acceleration is represented as

$$\begin{aligned} \boldsymbol{a} &= \sum_{j=1}^{3} a_j \hat{\boldsymbol{u}}_j + 2\sum_{j=1}^{3} v_j \Omega \times \hat{\boldsymbol{u}}_j + \sum_{j=1}^{3} x_j \frac{\mathrm{d}\Omega}{\mathrm{d}t} \times \hat{\boldsymbol{u}}_j + \sum_{j=1}^{3} x_j \Omega \times [\Omega \times \hat{\boldsymbol{u}}_j] \\ &= \sum_{j=1}^{3} a_j \hat{\boldsymbol{u}}_j + 2\Omega \times \sum_{j=1}^{3} v_j \hat{\boldsymbol{u}}_j + \frac{\mathrm{d}\Omega}{\mathrm{d}t} \times \sum_{j=1}^{3} x_j \hat{\boldsymbol{u}}_j + \Omega \times \left[\Omega \times \sum_{j=1}^{3} x_j \hat{\boldsymbol{u}}_j \right], \end{aligned} \tag{4.19}$$

Considering ourselves a co-moving observer rotating along with frame B (i.e. a corotating observer), let us define the apparent acceleration, velocity and position of the material point as

$$\boldsymbol{a}_{\mathrm{B}} = \sum_{j=1}^{3} a_j \hat{\boldsymbol{u}}_j \,, \qquad \boldsymbol{v}_{\mathrm{B}} = \sum_{j=1}^{3} v_j \hat{\boldsymbol{u}}_j \,, \qquad \boldsymbol{x}_{\mathrm{B}} = \sum_{j=1}^{3} x_j \hat{\boldsymbol{u}}_j \,, \tag{4.20}$$

Because the origins (0, 0) of the frames A and B coincide at all times t, for the position it holds that $\boldsymbol{x}_{\mathrm{B}} = \boldsymbol{x}$; these are the same vector (just expanded using different sets of basis vectors).

However, due to the rotating motion of frame B, for the velocity and the acceleration this is not the case. The apparent velocity (respectively, apparent acceleration) is

defined precisely to ignore the rotating motion of the frame, in order to give us the instantaneous velocity (resp. instantaneous acceleration) with respect to frame B as if frame B was stationary. In other words, $\boldsymbol{v}_{\mathrm{B}}$ (resp. $\boldsymbol{a}_{\mathrm{B}}$) represents the velocity (resp. acceleration), as seen by the co-rotating observer.

From equation (4.19), by inserting the definitions (4.20) and rearranging terms, we see that the apparent acceleration $\boldsymbol{a}_{\mathrm{B}}$ is related to the true physical acceleration $\boldsymbol{a}$ by

$$\boldsymbol{a}_{\mathrm{B}} = \boldsymbol{a} - 2\boldsymbol{\Omega}\times\boldsymbol{v}_{\mathrm{B}} - \boldsymbol{\Omega}\times(\boldsymbol{\Omega}\times\boldsymbol{x}_{\mathrm{B}}) - \frac{\mathrm{d}\boldsymbol{\Omega}}{\mathrm{d}t}\times\boldsymbol{x}_{\mathrm{B}}. \tag{4.21}$$

Let us denote the mass of the material point by m. Multiplying both sides of (4.21) by m and applying Newton's second law, we have

$$\boldsymbol{F}_{\mathrm{B}} = \boldsymbol{F} + \boldsymbol{F}_{\mathrm{fict}}. \tag{4.22}$$

On the left-hand side, $\boldsymbol{F}_{\mathrm{B}} = m\boldsymbol{a}_{\mathrm{B}}$ is the apparent total force that, for the co-rotating observer, appears to act on the material point. On the right-hand side, $\boldsymbol{F} = m\boldsymbol{a}$ is the true physical force acting on the material point, and $\boldsymbol{F}_{\mathrm{fict}}$ is the fictitious force,

$$\boldsymbol{F}_{\mathrm{fict}} = -2m\boldsymbol{\Omega}\times\boldsymbol{v}_{\mathrm{B}} - m\boldsymbol{\Omega}\times(\boldsymbol{\Omega}\times\boldsymbol{x}_{\mathrm{B}}) - m\frac{\mathrm{d}\boldsymbol{\Omega}}{\mathrm{d}t}\times\boldsymbol{x}_{\mathrm{B}}. \tag{4.23}$$

To explain, in the sense of Newton's second law, the behaviour of the material point in frame B, the co-rotating observer (considering his frame as stationary) must introduce this additional force.

In equation (4.23), on the right-hand side the first term represents the Coriolis effect, the second term the centrifugal effect, and the third term the Euler effect. Splitting $\boldsymbol{F}_{\mathrm{fict}}$ into these three contributions, we thus define

$$\boldsymbol{F}_{\mathrm{fict}} = \boldsymbol{F}_{\mathrm{cor}} + \boldsymbol{F}_{\mathrm{cf}} + \boldsymbol{F}_{\mathrm{Euler}}. \tag{4.24}$$

For the purposes of practical implementation of the drying cylinder problem, it is useful to obtain explicit component expressions for the three contributions to the fictitious force for the case of rotation around the z axis. First, let us consider the centrifugal term. We have

$$\boldsymbol{F}_{\mathrm{cf}} = -m\boldsymbol{\Omega}\times(\boldsymbol{\Omega}\times\boldsymbol{x}_{\mathrm{B}}) =: -m\boldsymbol{a}_{\mathrm{cf}}, \tag{4.25}$$

where $\boldsymbol{a}_{\mathrm{cf}}$ represents the centrifugal acceleration, to be determined. Let

$$\Omega := (\Omega_1, \Omega_2, \Omega_3), \tag{4.26}$$

$$\boldsymbol{x}_\mathrm{B} := (x_{\mathrm{B}1}, x_{\mathrm{B}2}, x_{\mathrm{B}3}), \tag{4.27}$$

$$\boldsymbol{S} := \Omega \times \boldsymbol{x}_B. \tag{4.28}$$

We have

$$\boldsymbol{S} = (S_1, S_2, S_3) = (\Omega_2 x_{\mathrm{B}3} - \Omega_3 x_{\mathrm{B}2}, \Omega_3 x_{\mathrm{B}1} - \Omega_1 x_{\mathrm{B}3}, \Omega_1 x_{\mathrm{B}2} - \Omega_2 x_{\mathrm{B}1}). \tag{4.29}$$

and

$$\boldsymbol{a}_\mathrm{cf} = \Omega \times (\Omega \times \boldsymbol{x}_\mathrm{B}) = \Omega \times \boldsymbol{S} = (\Omega_2 S_3 - \Omega_3 S_2, \Omega_3 S_1 - \Omega_1 S_3, \Omega_1 S_2 - \Omega_2 S_1). \tag{4.30}$$

Inserting (4.28) into (4.30), we obtain the result

$$\boldsymbol{a}_\mathrm{cf} = (a_x^\mathrm{cf}, a_y^\mathrm{cf}, a_z^\mathrm{cf}) = \begin{bmatrix} -(\Omega_2^2 + \Omega_3^2)x_{\mathrm{B}1} + \Omega_1\Omega_2 x_{\mathrm{B}2} + \Omega_1\Omega_3 x_{\mathrm{B}3} \\ \Omega_1\Omega_2 x_{\mathrm{B}1} - (\Omega_1^2 + \Omega_3^2)x_{\mathrm{B}2} + \Omega_2\Omega_3 x_{\mathrm{B}3} \\ \Omega_1\Omega_3 x_{\mathrm{B}1} + \Omega_2\Omega_3 x_{\mathrm{B}2} - (\Omega_1^2 + \Omega_2^2)x_{\mathrm{B}3} \end{bmatrix}. \tag{4.31}$$

In the special case of rotation around the z axis, i.e. $\Omega = (0, 0, \omega)$, we have

$$\boldsymbol{a}_\mathrm{cf} = \Omega \times (\Omega \times \boldsymbol{x}_\mathrm{B}) = (-\omega^2 x_{\mathrm{B}1}, -w^2 x_{\mathrm{B}2}, 0). \tag{4.32}$$

Hence, by (4.25), in this case the centrifugal fictitious force is

$$\boldsymbol{F}_\mathrm{cf} = -m\boldsymbol{a}_\mathrm{cf} = (m\omega^2 x_{\mathrm{B}1}, m\omega^2 x_{\mathrm{B}2}, 0), \tag{4.33}$$

which is seen to accelerate the object outward from the origin in the (x, y) plane (in frame B).

Next, consider the Coriolis force

$$\boldsymbol{F}_\mathrm{cor} = -2m\Omega \times \boldsymbol{v}_\mathrm{B} =: -2m\boldsymbol{a}_\mathrm{cor}. \tag{4.34}$$

Let

$$\boldsymbol{v}_B := (v_{\mathrm{B}1}, v_{\mathrm{B}2}, v_{\mathrm{B}3}). \tag{4.35}$$

Using (4.17), (4.26) and (4.35), we have

$$\boldsymbol{a}_{\mathrm{cor}} = \Omega \times v_{\mathrm{B}} = (\Omega_2 v_{\mathrm{B3}} - \Omega_3 v_{\mathrm{B2}},\ \Omega_3 v_{\mathrm{B1}} - \Omega_1 v_{\mathrm{B3}},\ \Omega_1 v_{\mathrm{B2}} - \Omega_2 v_{\mathrm{B1}}), \tag{4.36}$$

whence

$$a_{\mathrm{cor}} = (a_x^{\mathrm{cor}}, a_y^{\mathrm{cor}}, a_z^{\mathrm{cor}}) = \begin{bmatrix} \Omega_2 v_{\mathrm{B3}} - \Omega_3 v_{\mathrm{B2}} \\ \Omega_3 v_{\mathrm{B1}} - \Omega_1 v_{\mathrm{B3}} \\ \Omega_1 v_{\mathrm{B2}} - \Omega_2 v_{\mathrm{B1}} \end{bmatrix} = \begin{bmatrix} -\omega v_{\mathrm{B2}} \\ \omega v_{\mathrm{B1}} \\ 0 \end{bmatrix}. \tag{4.37}$$

The last form refers to the special case of rotation around the z axis. In that case, the Coriolis contribution to the fictitious force is thus

$$\boldsymbol{F}_{\mathrm{cor}} = -2m\boldsymbol{a}_{\mathrm{cor}} = (2m\omega v_{\mathrm{B2}}, -2m\omega v_{\mathrm{B1}}, 0). \tag{4.38}$$

It acts at a right angle (for $\omega > 0$, rotated clockwise) to the apparent velocity vector of the material point in frame B.

Finally, consider the Euler force, related to the angular acceleration of frame B:

$$\boldsymbol{F}_{\mathrm{Euler}} = -m\frac{\mathrm{d}\Omega}{\mathrm{d}t} \times \boldsymbol{x}_{\mathrm{B}} =: -m\boldsymbol{a}_{\mathrm{Euler}}. \tag{4.39}$$

Let $\Phi := \mathrm{d}\Omega/\mathrm{d}t$ (unit [1/s^2]), and denote its component representation by $\Phi = (\phi_1, \phi_2, \phi_3)$. Similarly to the above,

$$a_{\mathrm{Euler}} = (a_x^{\mathrm{Euler}}, a_y^{\mathrm{Euler}}, a_z^{\mathrm{Euler}}) = \begin{bmatrix} \phi_2 x_{\mathrm{B3}} - \phi_3 x_{\mathrm{B2}} \\ \phi_3 x_{\mathrm{B1}} - \phi_1 x_{\mathrm{B3}} \\ \phi_1 x_{\mathrm{B2}} - \phi_2 x_{\mathrm{B1}} \end{bmatrix} = \begin{bmatrix} -\phi x_{\mathrm{B2}} \\ \phi x_{\mathrm{B1}} \\ 0 \end{bmatrix}. \tag{4.40}$$

Again, the last form refers to the case of rotation around the z axis, and $\phi := \phi_3$. The Euler contribution to the fictitious force is obtained as

$$\boldsymbol{F}_{\mathrm{Euler}} = -m\boldsymbol{a}_{\mathrm{Euler}} = (m\phi x_{\mathrm{B2}}, -m\phi x_{\mathrm{B1}}, 0). \tag{4.41}$$

Mathematically the expression is similar to that of the Coriolis force, equation (4.38), but here the magnitude depends on ϕ, the angular acceleration of the cylinder, and the apparent velocity $\boldsymbol{v}_{\mathrm{B}}$ has been replaced by the position $\boldsymbol{x}_{\mathrm{B}}$. For steady-state operation, where ω remains constant in time (for any given cylinder), the Euler force vanishes.

To summarize, in the case of rotation around the z axis, equations (4.33), (4.38) and (4.41) provide the centrifugal, Coriolis and Euler contributions to the

fictitious force (4.24), which describes inertial effects in the rotating coordinate system. By adding this fictitious force to the physical external forces, the rotating coordinate system can be in all other respects treated as if it was an inertial one.

5 NUMERICAL RESULTS

In the simulations, we have considered two cases. First, we will look at the qualitative behaviour of the liquid water in an accelerating rotating cylinder starting from rest. Then, will we separately consider steady operation at the final speed of rotation, and investigate the effect of the thickness of the condensate layer on the heat absorbed from the steam by the liquid water.

5.1 Case with zero initial velocity

To begin with, we will show the capability of PFEM-2 for tracking the behaviour of the condensate in all the phases of an accelerating drying cylinder: starting from the puddle, moving through the cascade phase, and finally rimming. The domain consists on a cylinder with diameter $d = 2$ m and 30 turbulators, each with length $b = 4$ cm and height $h = 2$ cm.

In the initial state, the temperature of the water is 90 °C and the superheated steam 200 °C. The pressure inside the dryer is of 3 bar. The parameters of dry superheated steam have been used, and as was explained before, for the sake of simplicity, we neglect any phase changes from steam to condensate. Given these conditions, the steam must remain above 132 °C to avoid condensation.

We have chosen to smoothly increase the angular velocity of the simulated drying cylinder, using

$$\omega(t) = \frac{2}{\pi}\Omega_{\max}\arctan(St). \tag{5.1}$$

The corresponding angular acceleration is

$$\phi(t) \equiv \frac{\mathrm{d}\omega}{\mathrm{d}t}(t) = \frac{2}{\pi}S\Omega_{\max}\frac{1}{1+S^2t^2}. \tag{5.2}$$

where Ω_{max} is the maximum (target) angular velocity (in radians per second), and S is a smoothing factor (unit [1/s]) affecting the slope of the curve. Figure 5.1(e) shows the acceleration function with different smoothing factors $S \in [0, 2]$. In practice, there are many constraints in accelerating a paper machine to its full running speed, and the process can take significantly more time to complete than in this simulation.

Under these assumptions, heat conduction and convection have been solved. In the PFEM-2 method, as most FEM multiphase solvers, there are some challenges for conservation of mass, and a mass correction factor has been used in the computations to ensure that the total condensate mass remains constant throughout the simulation.

Figure 5.1 shows the behaviour of the condensate in the simulation as the cylinder accelerates. The behaviour follows what is known from the literature (see e.g. the schematic in Figure 2.1) and experiments. At the beginning of the simulation there is 20 cm of water at the bottom of the cylinder. The cylinder rotates counterclockwise, and accelerates based on equations (5.1) and (5.2), with the parameter values chosen as $\Omega_{max} = 10$ [1/s] and $S = 1$ [1/s].

It is known that heat exchange is efficient in the cascading phase (Fig. 5.1 (b)), but decreases rapidly in the rimming phase (Fig. 5.1 (c)). In Fig. 5.1 (d), we see the stable sloshing effect that occurs due to the combination of the centrifugal effect and gravity. Compared to videos from experiments, the qualitative behavior is captured correctly.

In Figure 5.2, one can observe the steam temperature evolution at different time steps. It is interesting to note that, while in the beginning of the process there is hot steam in contact with the water and therefore good heat transfer, in the latter stages a stratified field is observed with poor mixing between layers.

This result is in accordance with the physics of the problem. Due to the high angular velocity, the body forces are mostly oriented in the local radial direction at each point. The steam in direct contact with the condensate cools down, and therefore increases its density and thus reduces its buoyancy. These heavier structures shown in Figure 5.2(d) move and rotate slowly while always remaining close to the walls. On the other hand, the layers close to the center of the cylinder remain hotter, due to the low conductivity of the steam and negligible convective heat transfer.

The time evolution of the average water temperature at the dryer walls is shown in Figure 5.3. As expected, the temperature increase is initially high, when the pool is in contact with the hot steam, but later sees a reduction in the gradient. In order to determine if this inefficient heat transfer was caused by the colder steam or by low perturbations inside the condensate, we analyzed the temperature distribution along the depth of the condensate. Interestingly, we did not find a clear trend in the temperature distribution, showing only minor, random variations. This evidence, combined with the vigorous sloshing detected when the interface movement is observed, shows that the turbulators are effectively allowing an adequate heat transfer between the steam and the walls of the cylinder. It follows that the poor behaviour observed in the stable stage is mostly caused by the lack of mixing observed within the steam phase.

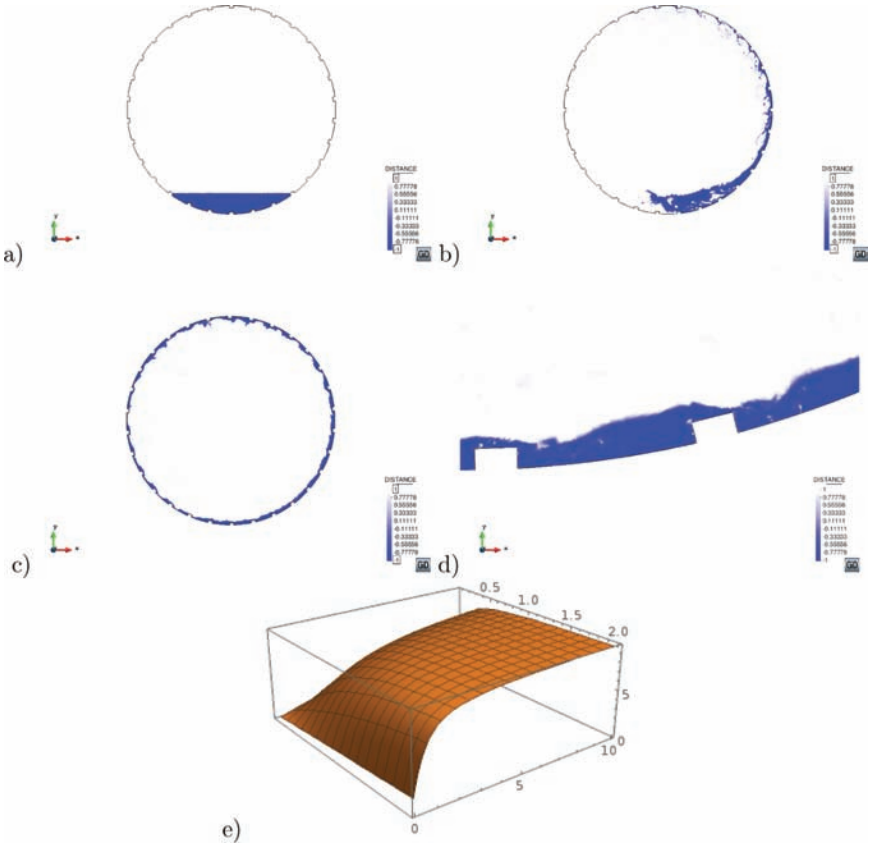

Figure 5.1. Phases of the accelerating drying cylinder. (a) Puddle phase ($t = 0.0025$ s). (b) Cascade phase ($t = 1.2$ s). (c) Rimming phase ($t = 3$ s). (d) Stable rimming phase, zoomed ($t = 20$ s). (e) Angular velocity of the drying cylinder, as prescribed by equation (5.1), as a function of the smoother parameter $S \in [0, 2]$ [1/s] and time $t \in [0, 10]$ [s]. The maximum angular velocity Ω_{max} is chosen to be 10 [1/s].

5.2 Measuring the effect of the condensate thickness

In order to assess the influence of the thickness of the condensate layer on the heat transfer process, two simulations were run with a different amount of liquid water. In order to avoid the long computational time required to reach the stationary state, the simulation starts directly at a constant angular velocity in the drum, and the condensate is homogeneously distributed in all the condensate pools using a constant thickness. A thickness of $\delta = 2.5$ cm is first simulated to evaluate normal

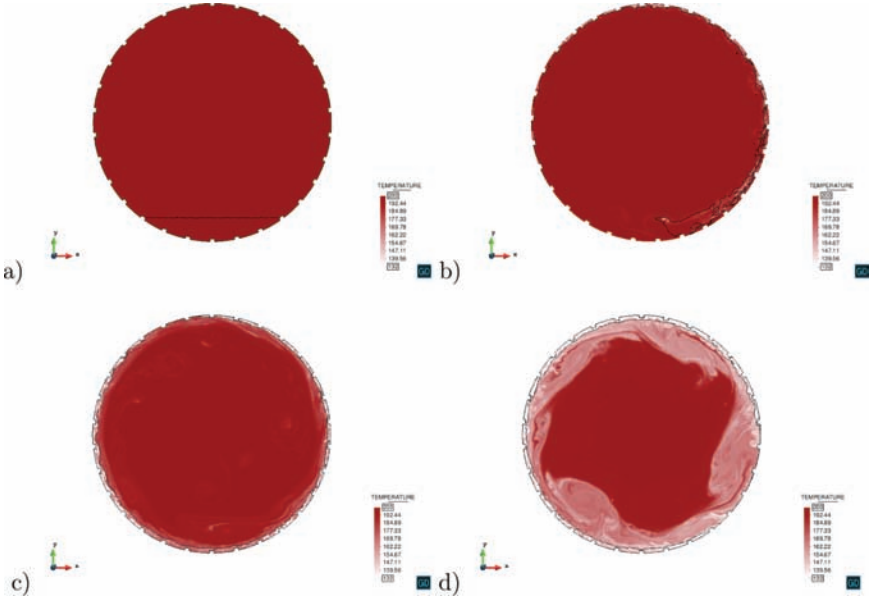

Figure 5.2. Temperature evolution of the accelerating drying cylinder. (a) Puddle phase ($t = 0.0025$ s). (b) Cascade phase ($t = 0.5$ s). (c) Rimming phase ($t = 3$ s). (d) Stable rimming phase ($t = 20$ s).

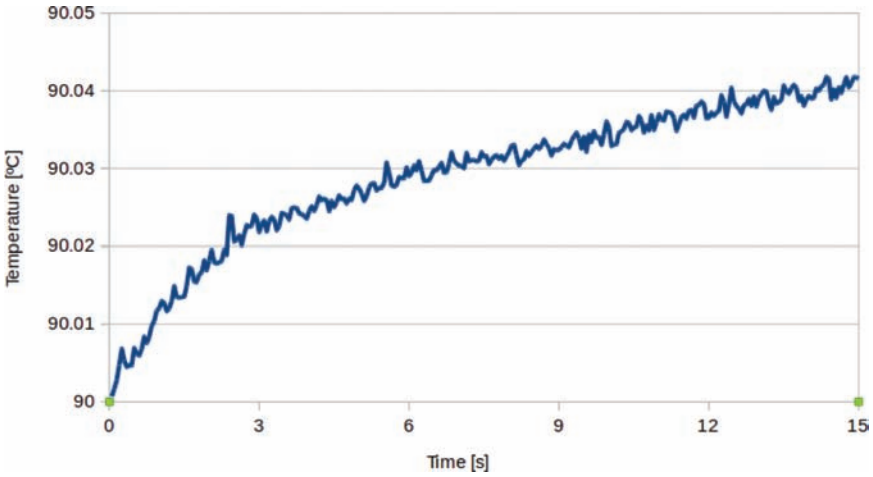

Figure 5.3. Time evolution of the average temperature at the cylinder walls.

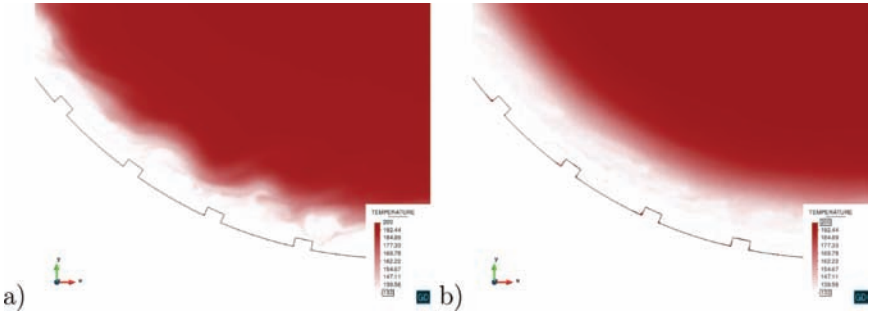

Figure 5.4. Snapshots at t = 15 s for different condensate thicknesses. (a) δ = 2.5 cm (b) δ = 5.0 cm.

working conditions. To test the same geometry under excessive condensate conditions, a thickness of δ = 5 cm is also simulated.

Unlike in the previous example, there is no startup phase for the rotation, and therefore there are less initial perturbations. This means that the steam phase disturbances are mostly caused by the sloshing within the condensate pools.

Snapshots at time t = 15 s are shown in Figure 5.4. The case of δ = 2.5 cm shows several structures (Figure 5.4(a)) in the temperature distribution, caused by the sloshing produced between the turbulators. On the other hand, the case of δ = 5 cm (Figure 5.4(b)) shows a stratified temperature field without important disturbances. This is due to the condensate layer being thicker than the turbulators, therefore severely reducing the sloshing.

In order to evaluate quantitatively the effect of the condensate thickness, Figure 5.5 shows the total heat absorbed by the liquid water phase in both cases. As it can be observed, both simulations show initially the same gradient. But, as the simulation advances and the steam layers become stratified, the case with h = 5 cm sees a dramatical reduction in the slope due to the lack of convection between layers.

6 CONCLUSIONS

In this article, we have presented the PFEM-2 method for solving a complex thermal problem in a rotating drying cylinder with a sloshing condensate barrier. We have shown that the simulation qualitatively captures the main behavior adequately, and the results are comparable to common knowledge of the case and videos from experiments. These simulations are only preliminary studies of the topic, and more precise analysis is still needed for quantitative reliable results. For

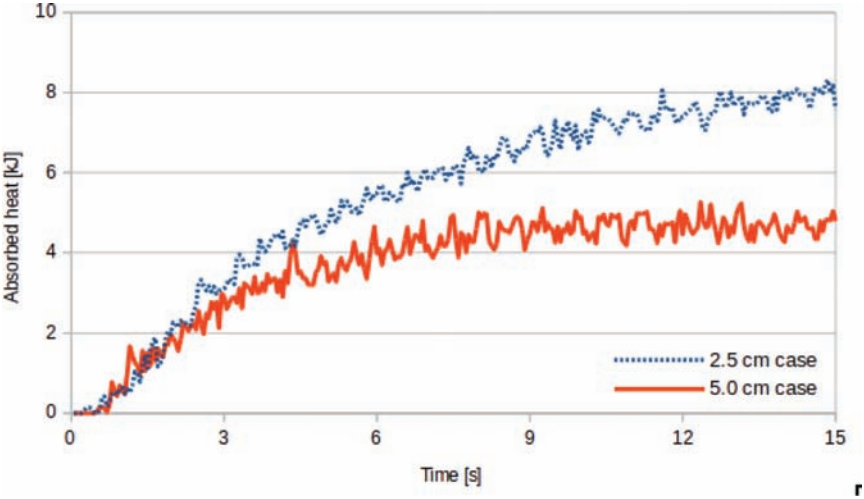

Figure 5.5. Heat absorbed by the water phase.

example, the phase change from steam to condensate was excluded, and only dry steam was considered. However, even with these simplifications, the qualitative behavior of the model is correct.

One of the main outcomes of the simulations was finding that it is important not only to ensure efficient mixing inside the condensate pools, but also within the steam, to ensure that an adequate heat flow occurs at the interface. This was a surprising result, given the fact that we were expecting the condensate to be the main limiting factor for an efficient heat transfer.

Finally, we estimated the thermal exchange out of the cylinder boundary using time-dependent analysis for two different thicknesses of the condensate layer. We found that the condensate layer smooths out the temperature profile at the outer boundary, and the effect is stronger for thicker layers. Also, as was expected, a thicker water barrier decreases the heat transfer significantly (40–60%). We also noticed that the sloshing effect, based on the interplay between gravity and the centrifugal effect in the rotating cylinder, is quite stable, at least when the thickness of the condensate layer is around 25 mm.

As a direction for future development, phase change and wet steam should be implemented into the algorithm. This would allow for a more realistic simulation of real drying cylinders. On the other hand, in our simulations we detected poor heat transfer due to the lack of renewal of steam, whereas in a real environment, steam would be constantly injected in the perpendicular direction, thus adding turbulence and possibly breaking the insulating steam layers close to the walls.

For this reason, 3D cases should be tested in order to correctly asses the mixing within the steam layer.

REFERENCES

1. D. Appel and S. Hong, "Optimizing heat-transfer using bars in dryers," *Paper Technology and Industry*, **16**(4): 264–269, 1975.
2. M. Lampinen, "Mechanics and Thermodynamics of Drying". PhD thesis, Helsinki University of Technology, 1979.
3. J. Pulkowski and G. Wedel, "The effect of spoiler bars on dryer heat transfer," *Pulp & Paper Canada*, **89**(8): 61–66, 1988.
4. B. Wilhemsson, *An Experimental and Theoretical Study of Multi-Cylinder Paper Drying*. McGill University, Montreal, Canada, 1994.
5. K. Juppi, "Experimental and Theoretical Study of the Effect of a New Dryer Construction on Paper Machine Runnability". PhD thesis, Helsinki University of Technology, 2001.
6. S. Peng, K. Mizukami, W. Liu, N. Sebe, and T. Takeba, "An experimental study of condensation heat transfer in a horizontally rotating cylinder with a scraper," *Experimental Thermal and Fluid Science*, **14**(2): 205–212, 1997.
7. S. Peng, "Theoretical analysis of laminar film condensation in a rotating cylinder with a scraper," *Heat and Mass Transfer*, **34**(4): 279–285, 1998.
8. K. Roonprasang, "Thermal Analysis of Multi-Cylinder Drying Section with Variant Geometry". PhD thesis, An der Fakultat Maschinenwesen der Technischen Universitat Dresden, 2008.
9. S. a. d. Wiesche, "Sloshing dynamics of a viscous liquid in a spinning horizontal cylindrical tank," *Aerospace Science and Technology*, **12**(6): 448–456, 2008.
10. M. Karlsson (ed.), *Papermaking Science and Technology Vol. 9: Papermaking Part 2: Drying*. Helsinki, Finland: Fapet Oy, 2000. ISBN 952-5216-09-8.
11. F. T. Dodge *et al.*, "The New "Dynamic Behavior of Liquids in Moving Containers". Southwest Research Inst. San Antonio, TX, 2000.
12. G. Wu, Q. Ma, and R. E. Taylor, "Numerical simulation of sloshing waves in a 3d tank based on a finite element method," *Applied Ocean Research*, **20**(6): 337–355, 1998.
13. B. Godderidge, S. Turnock, M. Tan, and C. Earl, "An investigation of multiphase CFD modelling of a lateral sloshing tank," *Computers & Fluids*, **38**(2): 183–193, 2009.
14. D. Lu, A. Takizawa, and S. Kondo, "Overflow-induced vibration of a weir coupled with sloshing in a downstream tank," *Journal of Fluids and Structures*, **11**(4): 367–393, 1997.
15. Z. Chen, X. Chen, and J. Chen, "Effects of an oscillating interface on heat transfer," *Chemical Engineering Science*, **52**(19): 3265–3275, 1997.
16. M. Joucaviel, L. Gosselin, and T. Bello-Ochende, "Maximum heat transfer density with rotating cylinders aligned in cross-flow," *International Communications in Heat and Mass Transfer*, **35**(5): 557–564, 2008.
17. S. R. Idelsohn, E. Oñate, and F. D. Pin, "The particle finite element method: a powerful tool to solve incompressible flows with free-surfaces and breaking waves," *International Journal for Numerical Methods in Engineering*, **61**(7): 964–989, 2004.

18. M. d. Mier-Torrecilla, S. Idelsohn, and E. Oñate, "Advances in the simulation of multi-fluid flows with the particle finite element method application to bubble dynamics," *International Journal for Numerical Methods in Fluids*, **67**(11): 1516–1539, 2011.
19. E. Oñate, A. Franci, and J. M. Carbonell, "A particle finite element method for analysis of industrial forming processes," *Computational Mechanics*, **54**(1): 85–107, 2014.
20. E. Oñate, A. Franci, and J. M. Carbonell, "A particle finite element method (PFEM) for coupled thermal analysis of quasi and fully incompressible flows and fluid structure interaction problems," in *Numerical Simulations of Coupled Problems in Engineering*, 129–156, Springer, 2014.
21. F. Salazar, J. Irazábal, A. Larese, and E. Oñate, "Numerical modelling of landslide generated waves with the particle finite element method (PFEM) and a non-Newtonian flow model," *International Journal for Numerical and Analytical Methods in Geomechanics*, 2015.
22. S. Idelsohn, N. Nigro, J. Gimenez, R. Rossi, and J. Marti, "A fast and accurate method to solve the incompressible Navier-Stokes equations," *Engineering Computations*, **30**(2): 197–222, 2013.
23. M. A. Valenzuela, J. M. Bentley, and R. D. Lorenz, "Estimation of condensate inside dryer cylinders during section shutdown," *IEEE Transactions on Industry Applications*, **50**: 1668–1677, May 2014.
24. R. A. Ibrahim, *Liquid Sloshing Dynamics: Theory and Applications*. Cambridge University Press, 2005.
25. M. Pereira, R. C. Valenzuela, and M. A. Valenzuela, "Experimental evaluation and modeling of condensate effects in dryer cylinders," in Pulp and Paper Industry Technical Conference, 2009. PPIC'09. Conference Record of 2009 Annual, 161– 170, IEEE, 2009.
26. R. Derrick, "Paper machine and winder drives," *Pulp and Paper Manufacture*, **7**: 525–547, 1991.
27. M. D. Concannon, "Condensate effects on torque and horsepower in paper dryers," *TAPPI – Journal of the Technical Association of the Pulp and Paper Industry* (USA), 1980.
28. G. Wedel and G. Timm, "Drive power and torque in paper machine dryers," in *Proc. Technol. Summit*, 1–8, 2002.
29. S. R. Idelsohn, E. Oñate, and F. del Pin, "A Lagrangian meshless finite element method applied to fluid–structure interaction problems," *Computers & Structures*, **81**(8–11): 655–671, 2003.
30. P. Becker, S. Idelsohn, and E. Oñate, "A unified monolithic approach for multifluid flows and fluid–structure interaction using the particle finite element method with fixed mesh," *Computational Mechanics*, **55**(6): 1091–1104, 2015.
31. A. L. Fetter and J. D. Walecka, *Theoretical Mechanics of Particles and Continua*. Courier Corporation, 2003.
32. R. D. Gregory, *Classical Mechanics*. Cambridge University Press, 2006.
33. J. Taylor, *Classical Mechanics*. University Science Books, 2005.

Transcription of Discussion

SIMULATION OF SLOSHING OF CONDENSATE WATER INSIDE A DRYING CYLINDER USING PARTICLE FINITE ELEMENT METHOD

Tero Tuovinen, Juha Jeronen and Pablo Becker

University of Jyväskylä, Mattilannniemi 2, Jyväskylä 40014, Finland

Daniel Söderberg KTH Royal Institute of Technology

This is a two-dimensional simulation. So, what are the implications of 3-D simulation, it's a turbulent case thus flows are typically three dimensional?

Juha Jeronen University of Jyväskylä

It is true that flows typically are three-dimensional. We have not yet moved into the 3-D case, what we wanted to do here was basically to set up a 2-D model and see how far that takes us. As you could see in the numerical results, this can already reproduce the qualitative stages of the behavior of the liquid water. However, you are right that there might be something interesting that could be seen by going into 3-D, that's maybe something for a future study.

Jean-Claude Roux Grenoble Institute of Engineering.

I was wondering if you have modelled a typical drying cylinder, with bars inside. I am not sure if you have bars inside your scheme, and my question is, did you simulate without bars and with bars, and what was the difference?

Discussion

Juha Jeronen

It is possible to do both, it just requires a change in the geometry. My co-author, Tero Tuovinen, did the simulations here. I am not sure if we did it without the bars, at least we simulated it with the bars.

Tero Tuovinen University of Jyväskylä

Yes. Let me comment about this. I tested this also without bars, but it was much more realistic looking with the bars.

Torbjörn Wahlström Stora Enso

I was taught many years ago that the turbulence bar, is one of those things where nature actually works with and not against us, in the way that they break up the formed ring [of condensate]. If we imagine that this ring just goes around the same speed as the cylinder, then the bars would not work once there are no relative motion between bar and water. However, I was told that the ring actually goes into an oscillating mode, creating a relative motion, and that is why the bars work. Furthermore, this oscillation is not dependent on the speed, which it can't be, because then the spacing would need to change, with the changed speed of the machine. Have you seen anything of this in your simulations?

Juha Jeronen

Yes, actually, and it is also in our full paper. As you said, the spacing of the bars does not depend on the rotational speed, it only depends on the thickness of the condensate layer that the cylinder is designed for. The cause behind this oscillation is that, as the cylinder rotates, effectively if you go into a co-rotating frame that rotates with the cylinder, then you will see that the gravity vector changes its direction all the time, and this is what causes the oscillation. Also there are inertial effects that must be taken into account. The condensate layer on the rim is formed because of the centrifugal effect, but the oscillation, I think it comes from the change in direction of the gravity vector as the cylinder rotates. Does this answer your question?

Torbjörn Wahlström

Yes, and you can confirm that the spacing of the bars does not depend on the speed of the machine?

Juha Jeronen

Yes, I confirm.

Wolfgang Bauer Graz University of Technology

If you look at your simulations, on the top of the turbulator bar it always appeared that the layer of water was thicker, or did I see this wrong?

Juha Jeronen

Actually, I didn't have any pictures here without bars. Do you mean this one? That is mostly the steam, whose temperature you can see here? The water layer is, as we can see here, at the bottom, and these are the bars. So the water layer may be slightly thicker than the bar height, but not that much. So the temperature field you can see in this picture mostly belongs to the stream.

Jose Iribarne WestRock

It is known that with nonlinear equations such as Navier-Stokes, the boundary conditions are very important, the so-called butterfly effect. So how much did you have to manipulate your boundary conditions to get stable results?

Juha Jeronen

My co-author did the simulation, but if I recall correctly we just used no-slip conditions. From a numerical standpoint, the advantage of using the co-rotating frame approach and fictitious forces is, that effectively your computational geometry is stationary. It is just like computing in a stationary geometry, but you just have some additional force terms and that makes the computation much simpler.

Tero Tuovinen

I confirm this.